Nanoscale

Accepted Manuscript

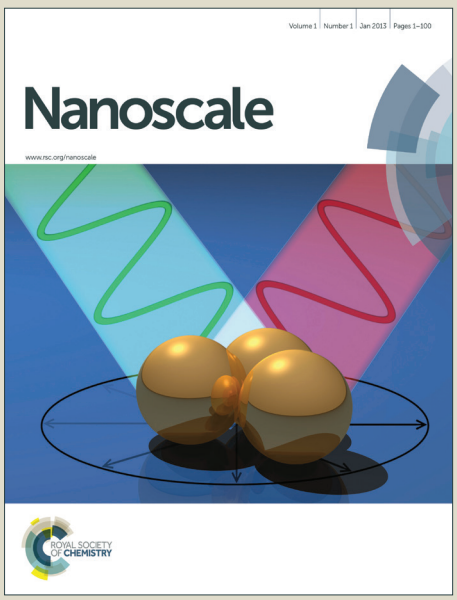

ROYAL SOCIETY OF CHEMISTRY

www.rsc.org/nanoscale

Journal Name

ARTICLE

Room-Temperature, Solution-Processable Organic Electron Extraction Layer for High-Performance Planar Heterojunction Perovskite Solar Cells

Received 00th January 20xx,
Accepted 00th January 20xx

DOI: 10.1039/x0xx00000x

www.rsc.org/

Jong H. Kim,[a,b] Chu-Chen Chueh,[a] Spencer T. Williams[a] and Alex K.-Y. Jen*[a,c]

In this work, we describe a room-temperature, solution-processable organic electron extraction layer (EEL) for high-performance planar heterojunction perovskite solar cells (PHJ PVSCs). This EEL is composed of a bilayered fulleropyrrolidinium iodide (FPI)-polyethyleneimine (PEIE) and $PC_{61}BM$, which yields a promising power conversion efficiency (PCE) of 15.7 % with insignificant hysteresis. We reveal that $PC_{61}BM$ can serve as a surface modifier of FPI-PEIE to simultaneously facilitate the crystallization of perovskite and the charge extraction at FPI-PEIE/ $CH_3NH_3PbI_3$ interface. Furthermore, the FPI-PEIE can also tune the work function of ITO and dope $PC_{61}BM$ to promote the efficient electron transport between ITO and $PC_{61}BM$. Based on the advantages of room-temperature processability and decent electrical property of FPI-PEIE/$PC_{61}BM$ EEL, a high-performance flexible PVSC with a PCE ~10% is eventually demonstrated. This study shows the potential of low-temperature processed organic EEL to replace transition metal oxide-based interlayers for highly printing compatible PVSCs with high-performance.

Introduction

To meet the continually growing global energy demand, the development of new photovoltaic materials with high light-to-energy conversion efficiency and sustainability has attracted significant attention from both researchers and commercial sectors.[1-5] Since the first perovskite solar cell (PVSC) reported in 2009, the hybrid organic-inorganic lead halide perovskites ($CH_3NH_3PbX_3$, X = Cl^-, Br^- or I^-) have emerged as a new class of light harvesters for solar energy generation.[6] It was unveiled that perovskites possess superior optoelectronic properties such as intense broad-band absorption, small exciton binding energy, high charge carrier mobility, and long charge diffusion length.[7-10] Due to these appealing features, the PVSC with a power conversion efficiency (PCE) exceeding 20.0 % has been realized recently, which is comparable to the performance of inorganic copper-indium-gallium-selenide (CIGS)- or silicon (Si)-based photovoltaics.[11-17] Moreover, perovskites possess simple solution-processability, showing great potential for low-cost, mechanically flexible, and light-weight solar cell applications.

In general, a PVSC consists of a perovskite light absorber sandwiched between selective electron- and hole-transporting layers (ETLs and HTLs). To find a simple and efficient way to process these charge-transporting interlayers is one of the main technical challenges impeding roll-to-roll printing of flexible devices.[18] For example, the most widely used inorganic titanium dioxide (TiO_2) ETL usually requires high-temperature (400-500°C) sintering after deposition to achieve high crystallinity.[13,19] Although several low-temperature processed TiO_2, zinc oxide (ZnO), or cadmium selenide (CdSe) nanostructures have been exploited to circumvent this problem,[20-22] synthesis of these materials often involves long reaction time and solvent washing process. These problems combined with difficulty in getting precise thickness control upon deposition pose the challenges for mass production.[23,24] Besides, potential variations in nanocrystal sizes also create discrepancies in the resultant photovoltaic performance. All these challenges might hinder the technology translation of PVSCs, in particular for printable flexible solar cells.

Compared to the inorganic ETLs, the low-cost, decent flexibility, and versatile deposition methods of organic semiconductors are advantageous to address the abovementioned challenges for achieving better printing compatibility. However, there are only very few suitable organic ETLs for high-performance PVSCs due to the lack of materials with high electrical conductivity, low-temperature, orthogonal solvent processability, and proper energy levels for

[a]Department of Materials Science and engineering, University of Washington, Seattle, WA, 98195-2120, USA. Email: ajen@u.washington.edu
[b]Department of Chemical Engineering Education, Chungnam National University, 99 Daehak-ro, Yuseong-gu, Daejeon, 305-764, South Korea.
[c]Department of Chemistry, University of Washington, Seattle, WA, 98195-1700, USA.

† Electronic Supplementary Information (ESI) available: AFM images, transfer characteristics of field-effect transistors and *J-V* curve for hysteresis measurement. See DOI: 10.1039/x0xx00000x

efficient electron extraction and cathode optimization. Therefore, it is imperative to develop rationally designed organic ETLs featuring these desirable properties for realizing low-cost printable PVSCs.

Among current state-of-the-art organic ETLs, fullerene derivatives have attracted the most attention.[25-27] In particular, fulleropyrrolidinium iodides (FPIs) have been effectively utilized as efficient cathode interfacial layers for tuning electrode work function (WF) and electron extraction in the solar cell devices. Due to their decent solution-processability and exceptionally high electrical conductivity, they can replace conventional cathode interfacial layers such as LiF, which usually requires high vacuum thermal evaporation process.[25-27] Most recently, Jen *et al.* have further blended a novel FPI derivative (Bis-OMe FPI) containing compact ammonium and methoxybenzene units with a very small amount of polyethyleneimine (PEIE) to form a stable and thickness-insensitive cathode interfacial layer, denoted as FPI-PEIE (Bis-OMe:PEIE = 125:1 w/w ratio). This layer has enabled an inverted organic solar cell to yield a high PCE of 9.6 %. More importantly, its self-doping character allows FPI-PEIE to maintain exceptionally high electrical conductivity for its efficient operation across a broad thickness range (16-50 nm), which is superior than the commonly used insulating polyelectrolyte interlayers such as PEIE or polyfluorene derivatives (PFNs) that can only be operated in thin thickness.

Furthermore, the FPI-PEIE can also dope the adjacent [6,6]-phenyl-C_{61}-butyric acid methyl ester ($PC_{61}BM$) in the bulk heterojunction (BHJ) layer to create highly conductive ETL/BHJ interface to enable efficient electron extraction in device.[28] It is worthwhile to note that the energy level between the FPI-PEIE-modified ITO (-3.91 eV, c.f. WFs are -4.07 and -3.84 eV for FPI/ITO and PEIE/ITO, respectively) and the conduction band (CB) of $CH_3NH_3PbI_3$ (-3.93 eV) is well aligned to minimize potential energy loss across the interface.[28,29] This combined with its facile room temperature solution-processability suggests that the conductive FPI-PEIE might also serve as an efficient electron extraction layer (EEL) for high-performance printable PVSCs.

In this study, we demonstrate a high-performance (PCE >15%) planar heterojunction (PHJ) PVSC by using a bilayered FPI-PEIE/$PC_{61}BM$ EEL. We reveal that a thin (50 nm) organic surface modifier, $PC_{61}BM$, is critically required, which not only facilitate the crystallization of atop perovskite thin films but also promote the charge extraction at the FPI-PEIE/$CH_3NH_3PbI_3$ interface. Meanwhile, the FPI-PEIE can simultaneously tune the WF of ITO and dope the $PC_{61}BM$ modifier to enable efficient electron transport between ITO and $PC_{61}BM$. As a result, the PHJ PVSC based on this EEL shows a promising PCE of 15.7 %. More importantly, the room-temperature processability and decent electric property of FPI-PEIE/ $PC_{61}BM$ EEL can also afford a flexible PVSC to show an impressive PCE of 10%. This study shows the potential of low-temperature processed organic EEL to replace transition metal oxide (TMO)-based interlayers for highly efficient PVSCs with better printing compatibility, representing an important step for the fabrication of low-temperature printable PVSCs.

Experiments

Materials

Methylammonium iodide (MAI) and Bis-OMe FPI were synthesized according to reported procedures [28,30]. Lead iodide (PbI_2), (2,2',7,7'-tetrakis(*N*,*N*-di-*p*-methoxyphenyl-amine)-9,9'-spirobifluorene (Spiro-OMeTAD), and $PC_{61}BM$ were purchased from Alfa Aesar, Borun Chemical and American Dye Source Inc, respectively.

Fabrication and characterization of perovskite solar cells

ITO-coated substrates (15 and 70 Ω/sq for glass and PET substrates, respectively) were used for the perovskite solar cells. Before device fabrication, the substrates were rinsed by sonication in detergent and deionized water, acetone and isopropyl alcohol for 10 min in sequence. After drying in a N_2 stream, the substrates were further cleaned by a plasma treatment for 30 s. Then the FPI-PEIE (Bis-OMe (2 mg/ml in methanol), Bis-OMe:PEIE=125:1 w/w ratio), $PC_{61}BM$ (10 mg/ml in chloroform) layers were sequentially spin-coated. Afterwards, the perovskite layer was spin-coated using 1.0 M $CH_3NH_3PbI_3$ solution in the mixed solvent of γ-butyrolactone and dimethyl sulfoxide (7:3, v/v ratio), followed by annealing on a hot plate at 100°C for 10 min (prior to spin-coating perovskite layer, the $PC_{61}BM$ surface was treated with 2-methoxy ethanol (4000 rpm, 30 s) to enhance its wettability with perovskite precursor solution). We have adopted the solvent-washing method reported by Seok et al. to optimize $CH_3NH_3PbI_3$ deposition.[14]

Spiro-OMeTAD (100 mg/mL) in chlorobenzene with 10 μL of 4-tert-butylpyridine and 42.9 μL of lithium-bis(trifluoromethylsulphonyl)imide (Li-TFSI, 0.61 M in acetonitrile) was spin-coated on top of perovskite film and then 100 nm-thick gold electrodes were thermal evaporated under a vacuum pressure of 5.0×10^{-7} Torr (with an evaporation rate of 0.5 Å s^{-1}) for hole extraction. The effective area of solar cells is 3.14 mm^2 defined by a mask. All the *J-V* curves in this study were measured using a Keithley 2400 source meter unit. The hysteresis of organic EEL-based solar cell was examined with a scan rate of 0.05 Vs^{-1}. The photocurrent of device was measured under the AM 1.5G illumination condition at an intensity of 100 mW cm^{-2}. The illumination intensity of the light source was accurately calibrated with a standard Si photodiode detector equipped with a KG-5 filter, which can be traced back to the standard cell of the National Renewable Energy Laboratory (NREL). A mask was used to define the effective illuminated area. The EQE spectra were obtained from incident photon-to-current conversion efficiency (IPCE) setup consisting of a Xenon lamp (Oriel, 450 W) as a light source, monochromator, a chopper with a frequency of 100 Hz, a lock-in amplifier (SR830, Stanford Research Corp), and Si-based diode (J115711-1-Si detector) for calibration.

Fabrication and characterization of field-effect transistors

$PC_{61}BM$ field-effect transistors were fabricated based on the

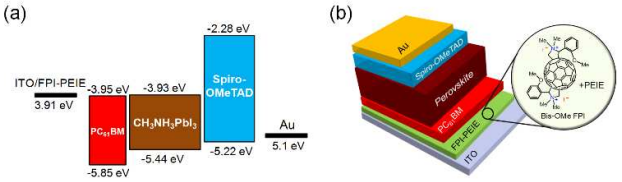

Figure 1. (a) Energy level diagram of the ITO/FPI-PEIE/$PC_{61}BM$/$CH_3NH_3PbI_3$/Spiro-OMeTAD/Au[27-29] and (b) device structure of perovskite solar cell based on FPI-PEIE/$PC_{61}BM$ electron extraction layer.

top-contact and bottom-gate geometry, with the configuration of *p*++Si/SiO_2/divinyltetramethyldisiloxane-bis(benzocyclobutene)(BCB)/$PC_{61}BM$/$CH_3NH_3PbI_3$/silver (Ag). Heavily doped *p*-type silicon substrates with a 300 nm-thick oxide layer were rinsed by sonication in acetone and isopropyl alcohol in sequence for 10 min and then treated by plasma for 1 min. After cleaning, the oxide dielectric was passivated with a cross-linked BCB layer to avoid electron trapping caused by surface hydroxyl groups. Afterward, $PC_{61}BM$ layers were spin-coated, followed by spin-coating of the $CH_3NH_3PbI_3$ layer. Finally, source and drain electrodes (channel width (*W*) = 1000 μm and channel length (*L*) = 50 μm) were defined by evaporating 50 nm-thick Ag layer through a shadow mask under vacuum pressure of 5.0×10^{-7} Torr with an evaporation rate of 2.0 Å s^{-1}. Transistors characterization was performed using an Agilent 4155B semiconductor parameter S6 analyzer. Electrical conductivity was derived from two-terminal measurement at zero gate voltage with the equation of $\sigma = (L/A)(I_{DS}/V_{DS})$, where *L* (cm) and *A* (cm^2) are the channel length and cross-sectional area of the devices, respectively.[28]

Results and Discussion

The multi-functions of FPI-PEIE interfacial layer in the solar cell device have been reported in our previous work. It can modify the WF of ITO from 4.60 eV to 3.91 eV to result in the well-aligned energy level with the CB (-3.93 eV) of $CH_3NH_3PbI_3$. Also, it can dope adjacent $PC_{61}BM$ to form Ohmic contact at the corresponding interface for better charge extraction efficiency.[28] Here, a $PC_{61}BM$ layer is sequentially spin-coated on top of this layer to constitute a bilayered EEL. This $PC_{61}BM$ layer was revealed to promote the perovskite crystallization and facilitate efficient electron extraction from the perovskite absorber due to its effective electronic coupling with perovskite. Note that the pristine electrical conductivity of $PC_{61}BM$ (1.98×10^{-9} Scm^{-1}) can be largely enhanced to 1.1×10^{-4} Scm^{-1} while using a bilayered FPI-PEIE/$PC_{61}BM$ due to the doping effects introduced by FPI-PEIE.[28] It is expected that this enhancement can facilitate the efficient charge extraction from perovskite when the FPI-PEIE/$PC_{61}BM$ serves as an EEL in the solar cell devices. In addition, by coating this $PC_{61}BM$ layer on top of FPI-PEIE, it allows orthogonal solvent to be used for processing perovskite film due to its resistance against polar solvents. The following section will elucidate the roles of this

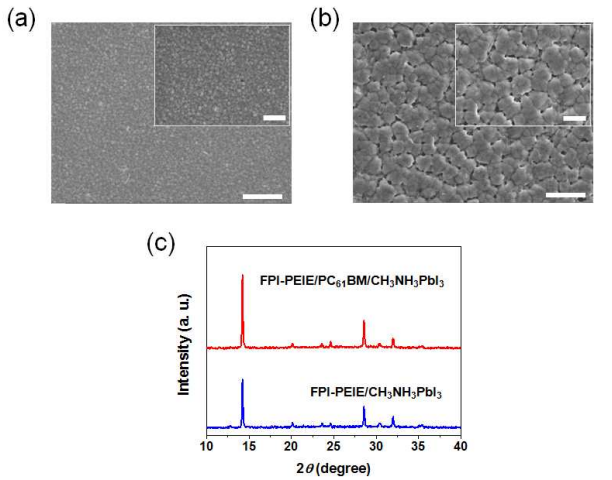

Figure 2. Scanning electron microscopy images of $CH_3NH_3PbI_3$ perovskite on FPI-PEIE (a) and on FPI-PEIE/$PC_{61}BM$ (b) (scale bars: 2 μm (1 μm for insets)). (c) X-ray diffraction spectra of $CH_3NH_3PbI_3$ perovskite layer on FPI-PEIE/$PC_{61}BM$ and FPI-PEIE.

FPI-PEIE/$PC_{61}BM$ EEL in enhancing device performance of PVSCs. It has been reported in the literature that crystal formation and perovskite surface morphology are strongly correlated with the surface energy and roughness of the underlying layers, which will have a significant influence on the ultimate performance of fabricated devices.[31,32] Similarly, the different surfaces of FPI-PEIE and FPI-PEIE/$PC_{61}BM$ EELs influences the perovskite crystallization and results in distinctly different surface morphologies of perovskite thin films, as can be seen in the scanning electron microscopy (SEM) images in **Figure 2a**,**b**. As discussed, this discrepancy might stem from the differences of surface morphology and roughness of the employed EELs. The images from atomic force microscopy (AFM) in **Figure S1** clearly show different surface structures and roughness of the employed EELs. Despite the relatively rough surface of FPI-PEIE/$PC_{61}BM$ layer, the perovskite on top of it clearly exhibits better grain coarsening compared to that grown directly on top of pristine FPI-PEIE. The perovskites deposited on top of FPI-PEIE/$PC_{61}BM$ showed much larger crystalline domains with grain size around 1 μm while perovskites grown on pristine FPI-PEIE exhibited relatively small crystalline domains of around 200 nm. Intense X-ray diffraction (XRD) signals also confirm the formation of crystalline $CH_3NH_3PbI_3$ films on both FPI-PEIE/$PC_{61}BM$ and FPI-PEIE, as shown in **Figure 2c**.[32,33]

Besides the influence from surface roughness, matched surface energy also plays an important role in forming proper perovskite films. Having a decent surface coverage of perovskite thin-film is a prerequisite for enhancing device performance, while the pinholes in the films will create electrical shorting and deteriorate device performance. In principle, the polar surface of ionic FPI-PEIE has a better compatibility with the perovskite precursor solution in the mixed solvent of γ-butyrolactone and dimethyl sulfoxide compared to the hydrophobic surface of $PC_{61}BM$. The incompatibility between perovskite and $PC_{61}BM$ will create an

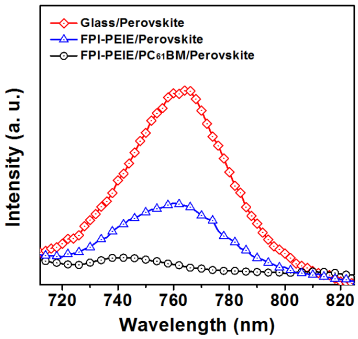

Figure 3. Photoluminescence spectra of $CH_3NH_3PbI_3$ perovskite films on top of bare glass (diamonds), FPI-PEIE (triangles) and FPI-PEIE/$PC_{61}BM$ (circles). Perovskite excitation wavelength was at 600 nm.

inferior surface coverage of perovskite layer. However, this issue can be effectively mitigated by pre-treating the surface of $PC_{61}BM$ with a polar solvent (2-methoxy ethanol) to facilitate the formation of highly uniform perovskite thin-films with larger crystalline domains (**Figure 2b**) for device investigation.

In order to investigate the photo-generated charge extraction efficiency of the FPI-PEIE/$PC_{61}BM$ layer from perovskite, photoluminescence (PL) quenching of the perovskite emission was measured. For fair comparison, PL quenching of FPI-PEIE/$CH_3NH_3PbI_3$ and FPI-PEIE/$PC_{61}BM$/$CH_3NH_3PbI_3$ films were measured and compared at the same time. As shown in **Figure 3**, the $CH_3NH_3PbI_3$ film shows a significant degree of PL quenching on FPI-PEIE/$PC_{61}BM$ compared to that on pristine FPI-PEIE, indicating enhanced electron extraction/transport efficiency of the FPI-PEIE/$PC_{61}BM$ layer. This demonstrates better viability of FPI-PEIE/$PC_{61}BM$ relative to FPI-PEIE as an effective EEL in PVSCs.[31]

In order to explore the efficacy of these EELs in PVSCs, devices with the configuration of ITO/organic EEL/$CH_3NH_3PbI_3$/Spiro-OMeTAD/Au were fabricated as depicted in **Figure 1b**. The current density-voltage (*J-V*) characteristics of devices under AM 1.5 G conditions (100 mW cm^{-2}) are shown in **Figure 4a**, and their relevant photovoltaic parameters are summarized in **Table 1** (average values with standard deviations were obtained from seven tested devices). As shown, the FPI-PEIE/$PC_{61}BM$-derived PVSC delivers a promising PCE of 15.7 %

Table 1 Summarized solar cell parameters of perovskite solar cells (average values with standard deviation (maximum values are indicated in the parentheses)

	V_{OC} [V]	FF	J_{SC} [$mAcm^{-2}$]	PCE [%]
FPI-PEIE	0.70 ± 0.03	0.24 ± 0.02	14.1 ± 0.40	2.34 ± 0.22 (2.62)
FPI-PEIE/ $PC_{61}BM$	1.09 ± 0.01	0.70 ± 0.02	19.2 ± 0.40	14.7 ± 0.65 (15.7)
Flexible Cell	1.07 ± 0.01	0.53 ± 0.01	17.8 ± 0.15	9.96 ± 0.06 (10.0)

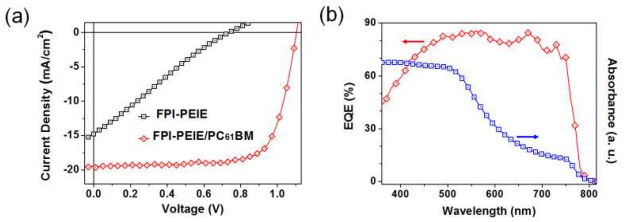

Figure 4. (a) *J–V* characteristics of $CH_3NH_3PbI_3$ solar cell based on FPI-PEIE/$PC_{61}BM$ (diamonds) and FPI-PEIE (squares). (b) Absorbance spectra of $CH_3NH_3PbI_3$ on FPI-PEIE/$PC_{61}BM$ (squares) and external quantum efficiency spectra of the corresponding device (diamonds).

with an open circuit voltage (V_{OC}) of 1.10 V, a short circuit current density (J_{SC}) of 19.5 mA cm^{-2} and a fill factor (FF) of 0.73 while the FPI-PEIE-derived PVSC only shows an inferior PCE of 2.62 % with much lower photovoltaic parameters. This difference can be clearly interpreted as a consequence of the increased perovskite crystallinity and enhanced charge extraction capability as abovementioned. Impressively, the high PVSC shows there is only minor potential loss since the optical badgap (E_g) of perovskite is around 1.51 eV. This affirms that FPI-PEIE/$PC_{61}BM$ can minimize photo-voltage loss pathways across the EEL/perovskite interface due to a synergetic result of effective ITO WF tuning by FPI-PEIE and enhanced charge transfer by $PC_{61}BM$. The external quantum efficiency (EQE) spectrum plotted in **Figure 4b** shows very high photon-to- electron conversion efficiency in the PVSC employing the FPI-PEIE/$PC_{61}BM$ layer, in which the maximum EQE peak reaches over 85% (The photocurrent value estimated from the EQE spectrum is 18.9 mA cm^{-2}, comparable to the value obtained from *J-V* curve with 3.08 % deviation). This result combined with the panchromatic absorption over the visible range (**Figure 4b**) features efficient light harvesting and charge extraction in PVSCs using organic EEL.

We have further examined the electrical property at the $PC_{61}BM$/$CH_3NH_3PbI_3$ interface using organic field-effect transistors (OFETs) to elucidate the role of $PC_{61}BM$ on the enhanced charge transfer observed at this corresponding interface. We first examined the *n*-type semiconducting characteristics of pristine $PC_{61}BM$ and then studied the bilayered $PC_{61}BM$/$CH_3NH_3PbI_3$ (FET based on pristine $CH_3NH_3PbI_3$ was also fabricated as a reference device, as presented in **Figure S2**). As shown in **Figure 5**, the electrical characteristics of $PC_{61}BM$ were dramatically changed after depositing perovskite on top of it. Originally, $PC_{61}BM$ exhibited typical *n*-type behavior with an off-current of ~10^{-11} A and an on/off ratio of 10^6. Its electrical conductivity at zero gate voltage was estimated to be 2.2 × 10^{-9} S cm^{-1}. However, after depositing a perovskite layer on top of $PC_{61}BM$, the device showed a considerable increased off-current and decreased on/off ratio, indicating an increased carrier concentration in the bulk film after $PC_{61}BM$ contacted with $CH_3NH_3PbI_3$. The electrical conductivity of the $PC_{61}BM$/$CH_3NH_3PbI_3$ bilayer at zero gate voltage was significantly improved to 4.0 × 10^{-5} S cm^{-1}, suggesting the formation of metallic electrical contact at the $PC_{61}BM$/perovskite interface.[28,34] This significantly enhanced electrical conductivity shows that the interfacial interactions

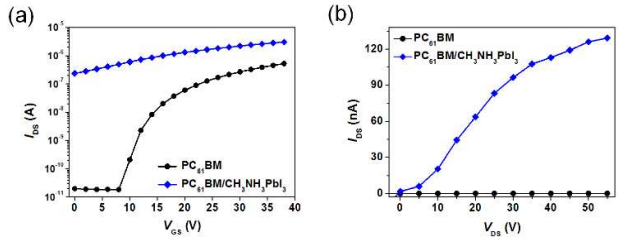

Figure 5. (a) Transfer characteristics of field-effect transistors based on pristine $PC_{61}BM$ (circles) and $PC_{61}BM/CH_3NH_3PbI_3$ (diamonds), and (b) output characteristics of field-effect transistors based on pristine $PC_{61}BM$ (circles) and $PC_{61}BM/ CH_3NH_3PbI_3$ (diamonds) at zero gate voltage.

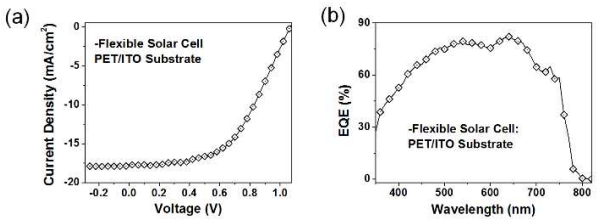

Figure 6. *J–V* characteristics (a) and external quantum efficiency spectrum (b) of $CH_3NH_3PbI_3$ solar cell based on PET/ITO substrate.

between $PC_{61}BM$ and $CH_3NH_3PbI_3$ play an important role in optimizing the electrical contact (or electronic coupling) and electron extraction (or charge transfer) at the FPI-PEIE/$CH_3NH_3PbI_3$ interface. The possible interactions might result from the passivation function of fullerene or the effective electronic coupling between them.[35-37] The detailed discussion regarding the correlation between fullerene-based interlayers and perovskite in PVSC based on X-ray photoelectron spectroscopy (XPS) and FET analyses has been reported elsewhere.[37]

Recently, the hysteresis found in PVSC devices has raised critical concern for the accuracy in device performance, especially for those employing the TMO-based ETLs. One of the possible causes for hysteresis might come from the interfacial trap states at the perovskite/interfacial layers. As shown in **Figure S3**, the device employing FPI-PEIE/$PC_{61}BM$ layer exhibits insignificant hysteresis, which is consistent with the general observation of reduced hysteresis found in conventional perovskite solar cells when highly conductive poly(3,4-ethylene-dioxythiophene):poly(4-styrenesulfonate) (PEDOT:PSS) HTL is used.[38] This result signifies the importance of the conductive FPI-PEIE interlayer, which can dope the adjacent $PC_{61}BM$ layer to enhance the overall conductivity of this bilayered EEL and reduce the trap states simultaneously to inhibit device hysteresis.[28]

Considering the roles of the components in this studied EEL, $PC_{61}BM$ layer indeed is the most crucial factor to achieve the high PCE, as discussed above. However, the interface between $PC_{61}BM$ and ITO also plays an important role in the resultant device performance. It has been revealed that the photovoltaic performance and hysteresis of the device might be closely correlated with the electric properties of this corresponding interface.[39] For example, it has been reported that n-i-p heterojunction perovskite solar cell using ZnO/$PC_{61}BM$ bilayered EEL shows improved device performance compared to the devices only using a $PC_{61}BM$ layer due to the better energy level alignment at the ITO/$PC_{61}BM$ interface.[40] Because of this energy level mismatch at the ITO/$PC_{61}BM$ interface, our control solar cell device using a single $PC_{61}BM$ layer as an EEL shows an inferior photovoltaic performance as shown in Figure S4. This result is in good accordance with the results reported in the literature,[40] which affirms the importance of the bilayered FPI-PEIE/$PC_{61}BM$ EEL. In addition, it has been shown that perovskite solar cell based on a bilayered PEIE/$PC_{61}BM$ EEL exhibits significant hysteresis despite exhibiting high PCE.[41] Intriguingly, our device using FPI-PEIE/$PC_{61}BM$ EEL exhibited comparable high PCE to the value of this PEIE/$PC_{61}BM$-based PVSC but showed a greatly reduced hysteresis, revealing the significant role of FPI-PEIE in yielding reliable device performance.

All these results combined with its room-temperature and solution processability greatly reveal the promising advantages of organic EEL. It not only can replace the TMO-based ETL to simplify the device fabrication but also have a better compatibility with roll-to-roll printing technique.

Two challenging issues mainly encountered in developing high-performance flexible PVSCs are to reduce the processing temperature of charge transport layers (CTLs) because of the instability of the plastic substrates at high temperatures and to achieve uniform CTL's morphologies and its decent electrical performance. Efforts have been made to address these issues to achieve efficient flexible PVSCs by a few groups. At present, 6.3~9.2% PCEs were accomplished in the PEDOT:PSS-based p-i-n configurations, for which 120~150^{o}C annealing processes are still required.[42,43] Meanwhile, n-i-p structured cells based on low-temperature processed inorganic nanocrystals exhibited 2.62~10.2% PCEs; however the performance of these cells are sensitively influenced by the thickness or morphology of the crystals.[44,45] Considering the exceptional advantages of FPI-PEIE/$PC_{61}BM$ EEL such as low-temperature solution processability and superior electrical properties, this layer is highly feasible to meet all these challenging requirements for developing high-performance flexible PVSCs. To test this, we fabricated PVSC using the FPI-PEIE/$PC_{61}BM$ EEL on ITO-coated poly(ethylene terephthalate) (PET) substrate (PET/ITO), and its *J-V* and EQE curves are shown in Figure 6. Encouragingly, a promising PCE of 10.0% (V_{OC}: 1.07V, J_{SC}: 17.7mA cm^{-2} and FF: 0.53) was achieved, which is comparable to the high PCEs of flexible PVSCs reported to date. Compared to the glass/ITO device, the PET/ITO device possessed lower J_{SC} and FF, which is apparently attributed to the higher sheet resistance of the flexible substrates.[28,46] Studies on further improving flexible PVSCs by using ITO-free, low-sheet resistance ultrathin metal electrodes are in progress.[47]

Conclusions

In summary, we have demonstrated a simple but efficient organic bilayered FPI-PEIE/$PC_{61}BM$ EEL with facile room-temperature solution-processability, which can successfully replace the conventional TMO-based ETL in *n-i-p* PHJ PVSCs.

We revealed that the $PC_{61}BM$ serves as a surface modifier of FPI-PEIE to simultaneously facilitate the crystallization of atop perovskite thin films and the charge extraction at FPI-PEIE/$CH_3NH_3PbI_3$ interface. Meanwhile, the FPI-PEIE can tune the work function of ITO and dope $PC_{61}BM$. As a result, the PVSC using this unique organic EEL yields a promising PCE of 15.7%. Moreover, providing its room-temperature processability and decent electrical property, a high-performance flexible PVSC with a PCE of 10 % is also achieved. This study demonstrates a new and simple platform for room-temperature, printable perovskite solar cells.

Acknowledgements

This material is based in part upon work supported by the State of Washington through the University of Washington Clean Energy Institute. The authors thank the support from the Asian Office of Aerospace R&D (No. FA2386-11-1-4072), the Department of Energy SunShot (DE-EE0006710), and the Office of Naval Research (No. N00014-14-1-0246). A. K.-Y. Jen thanks the Boeing Foundation for support. S.T.Williams thanks the financial support from National Science Foundation Graduate Research Fellowship Program (No. DGE-1256082).

Notes and references

1 K.L. Chopra, P.D. Paulson, V. Dutta, *Prog. Photovoltaics* 2004, **12**, 69-92.
2 B. Oregan, M. Grätzel, *Nature* 1991, **353**, 737-740.
3 M. Law, L.E. Greene, J.C. Johnson, R. Saykally, P.-D. Yang, *Nat. Mater.* 2005, **4**, 455-459.
4 G. Li, V. Shrotriya, J. Huang, Y. Yao, T. Moriaty, K. Emery, Y. Yang, *Nat. Mater.* 2005, **4**, 864-868.
5 G. Li, R. Zhu, Y. Yang, *Nat. Photon.* 2012, **63**, 153-161.
6 A. Kojima, K. Teshima, Y. Shirai, T. Miyasaka, *J. Am. Chem. Soc.* 2009, **131**, 6050-6051.
7 M. Grätzel, *Nat. Mater.* 2014, **13**, 838-842.
8 C.R. Kagan, D.B. Mitzi, C.D. Dimitrakopoulos, *Science* 1999, **286**, 945-947.
9 S.D. Stranks, G.E. Eperon, G.Grancini, C.Menelaou, M.J.P. Alcocer, T. Leijtens, L.M. Herz, A. Petrozza, H.J. Snaith, *Science* 2013, **342**, 341-344.
10 G. Xing, N. Mathews, S. Sun, S.-S. Lim, Y.-M. Lam, M. Grätzel, S. Mhaisalkar, T.-C. Sum, *Science* 2013, **342**, 344-347.
11 J. Burschka, N. Pellet, S.-J. Moon, R. Humphry-Baker, P. Gao, M.K. Nazeeruddin, M. Grätzel, *Nature* 2013, **499**, 316-319.
12 M. Liu, M.B. Johnston, H.J. Snaith, *Nature* 2013, **501**, 395-398.
13 J. H. Heo, S.H. Im, J.H. Noh, T.N. Mandal, C.-S. Lim, J.A. Chang, Y.H. Lee, H.-J. Kim, A. Sarkar, M.K. Nazeeruddin, M. Grätzel, S.I. Seok, *Nat. Photon.* 2013, **7**, 486-489.
14 N.J. Jeon, J.H. Noh, Y.C. Kim, W.S. Yang, S. Ryu, S.I. Seok, *Nat. Mater.* 2014, **13**, 897-903.
15 H.-S. Kim, C.-R. Lee, J.-H. Im, K.-B. Lee, T. Moehl, A. Marchioro, S.-J. Moon, R. Humphry-Baker, J.-H. Yum, J.E. Moser, M. Grätzel, N.-G. Park, *Sci. Rep.* 2012, **2**, 591.
16 M.A. Green, A. Ho-Baillie, H.J. Snaith, *Nat. Photon.* 2014, **8**, 506-514.
17 H. Zhou, Q. Chen, G. Li, S. Luo, T.-B. Song, H.-S. Duan, Z. Hong, J. You, Y. Liu, Y. Yang, *Science* 2014, **345**, 542-546.
18 C.-C.Chueh, C.-Z. Li, A.K.Y. Jen, *Energy Environ. Sci.* 2015, **8**, 1160-1189
19 Q. Hu, J. Wu, C. Jiang, T. Liu, X. Que, R. Zhu, Q. Gong, *ACS Nano* 2014, **8**, 10161-10167.
20 K. Wojciechowski, M. Saliba, T. Leijtens, A. Abate, H.J. Snaith, *Energy Environ. Sci.* 2014, **7**, 1142-1147.
21 D. Liu, T. L. Kelly, *Nat. Photon.* 2014, **8**, 133-138.
22 L. Wang, W. Fu, Z. Gu, C. Fan, X. Yang, H. Li, H. Chen, *J. Mater. Chem. C* 2014, **2**, 9087-9090.
23 J. Kim, G. Kim, T.-K. Kim, S. Kwon, H. Back, J. Lee, S.-H. Lee, H. Kang, K. Lee, *J. Mater. Chem. A* 2014, **2**, 17291-17296.
24 W.J.E. Beek, M.M. Wienk, M. Kemerink, X. Yang, R.A.J. Jassen, *J. Phys. Chem. B* 2005, **109**, 9505-9516.
25 Z.A. Page, Y. Liu, V.V. Duzhko, T.P. Russell, T.Emrick, *Science* 2014, **346**, 441-444.
26 C.-Z. Li, C.-C. Chueh, H.-L. Yip, K.M. O'Malley, W.-C. Chen, A.K.Y. Jen, *J. Mater. Chem.* 2012, **22**, 8574-8578.
27 K. M. O'Malley, C.-Z. Li, H.-L. Yip, A.K.Y. Jen, *Adv. Energy. Mater.* 2012, **2**, 82-86.
28 C.-Z. Li, C.-Y. Chang, Y. Zang, H.-X. Ju, C.-C. Chueh, P.-W. Liang, N. Cho, D.S. Ginger, A.K.Y. Jen, *Adv. Mater.* 2014, **26**, 6262-6267.
29 N.J. Jeon, H.G. Lee, Y.C. Kim, J. Seo, J.H. Noh, J. Lee, S.I. Seok, *J. Am. Chem. Soc.* 2014, **136**, 7837-7840.
30 P.-W. Liang, C.-Y. Liao, C.-C. Chueh, F. Zuo, S. T. Williams, X.-K. Xin, J. Lin, A.K.Y. Jen, *Adv. Mater.* 2014, **26**, 3748-3754.
31 P. Docampo, J.M. Ball, M. Darwich, G. Eperon, H.J. Snaith, *Nat. Commun.* 2013, **4**, 1.
32 Z. Xiao, W. Dong, C. Bi, Y. Saho, Y. Yuan, J. Huang, *Adv. Mater.* 2014, **26**, 6503-6509.
33 M. M. Lee, J. Teuscher, T. Miyasaka, T.N. Murakami, H.J. Snaith, *Science* 2012, **338**, 643-647.
34 C.-Z. Li, C.-C. Chueh, H.-L. Yip, F. Ding, X. Li, A.K.Y. Jen, *Adv. Mater.* 2013, **25**, 2457-2461.
35 Y. Shao, Z. Xiao, C. Bi, Y. Yuan, J. Huang, *Nat. Commun.* 2014, **5**, 5784.
36 M.-F. Lo, Z.-Q. Guan, T.-W. Ng, C.-Y. Chan, C.-S. Lee, *Adv. Funct. Mater.* 2015, **25**, 1213-1218.
37 P.-W. Liang, C.-C. Chueh, S.-T. Williams, A.K.Y. Jen, *Adv. Energy. Mater.* 2015, **5**, 1402321.
38 Z. Xiao, C. Bi, Y. Saho, Q. Dong, Q. Wang, Y. Yuan, C. Wang, Y. Gao, J. Huang, *Energy Environ. Sci.* 2014, **7**, 2619-2623.
39 A. K. Jena, H.-W. Chen, A. Kogo, Y. Sanehira, M. Ikegami, T. Miyasaka, *ACS Appl. Mater. Interfaces*, 2015, **7**, 9817-9823.
40 J. Kim, G. Kim, T. K. Kim, S. Kwon, H. Back, J. Lee, S. H. Lee, H. Kang, K. Lee, *J. Mater. Chem. A*, 2014, **2**, 172291-17296.
41 S. Ryu, J. Seo, S. S. Shin, Y. C. Kim, N. J. Jeon, J. H. Noh, S. I. Seok, *J. Mater. Chem. A*, 2015, **3**, 3271-3275.
42 P. Docampo, J. M. Ball, M. Darwich, G. E. Eperon, H. J. Snaith, *Nat. Commun.*, 2013, **4**, 2761.
43 J. You, Z. Hong, Y. Yang, Q. Chen, M. Cai, T.-B. Song, C.-C. Chen, S. Lu, Y. Liu, H. Zhou, Y. Yang, *ACS Nano*, 2014, **8**, 1674-1680.
44 M. H. Kumar, N. Yantara, S. Dharani, M. Grätzel, S. Mhaisalkar, P. P. Boix, N. Mathews, *Chem. Commun.*, 2013, **49**, 11089-11091.
45 D. Liu, T. L. Kelly, *Nat. Photon.*, 2014, **8**, 133-138.
46 K.-G. Lim, H.-B. Kim, J. Jeong, H. Kim, J.-Y. Kim, T.-W. Lee, T.-W. *Adv. Mater.* 2014, 26, 6461-6466.
47 J. Zou, C.-Z. Li, C.-Y. Chang, H.-L. Yip, A.K.Y. Jen, *Adv. Mater.* 2014, **26**, 3618-3623.